Spin waves in the ferromagnetic ground state of the kagome staircase system $Co_3V_2O_8$

M. Ramazanoglu,[1] C. P. Adams,[1,2] J. P. Clancy,[1] A. J. Berlinsky,[1,3] Z. Yamani,[4] R. Szymczak,[5] H. Szymczak,[5] J. Fink-Finowicki,[5] and B. D. Gaulin[1,3]

[1]*Department of Physics and Astronomy, McMaster University, Hamilton, Ontario, Canada L8S 4M1*

[2]*Department of Physics, St. Francis Xavier University, Antigonish, Nova Scotia, Canada B2G 2W5*

[3]*Canadian Institute for Advanced Research, 180 Dundas Street West, Toronto, Ontario, Canada M5G 1Z8*

[4]*Canadian Neutron Beam Centre, National Research Council, Chalk River Laboratories, Chalk River, Ontario, Canada K0J 1P0*

[5]*Institute of Physics, Polish Academy of Sciences, 02-668 Warsaw, Poland*

(Received 25 October 2008; published 15 January 2009)

Inelastic neutron-scattering measurements were performed on single-crystal $Co_3V_2O_8$ wherein magnetic cobalt ions reside on distinct spine and cross-tie sites within kagome staircase planes. This system displays a rich magnetic phase diagram which culminates in a ferromagnetic ground state below $T_C \sim 6$ K. We have studied the low-lying magnetic excitations in this phase within the kagome plane. Despite the complexity of the system at higher temperatures, linear spin-wave theory describes most of the quantitative detail of the inelastic neutron measurements. Our results show two spin-wave branches, the higher energy of which displays finite spin-wave lifetimes well below T_C, and that, surprisingly, the magnetic exchange coupling between Co moments on the spine sites is negligible.

DOI: 10.1103/PhysRevB.79.024417 PACS number(s): 75.30.Ds, 75.10.Dg, 75.50.Dd

I. INTRODUCTION

Magnetic materials in which the constituent magnetic moments reside on networks of triangles and tetrahedra have been of great interest due to their propensity for exotic ground states, a consequence of geometrical frustration.[1] While ferromagnetically coupled moments on such lattices generally do not result in such ground states, ferromagnets, and materials which display both ferromagnetic (FM) and antiferromagnetic (AFM) interactions, on such lattices remain of great interest in part due to the relative scarcity of well-studied examples and in part due to intriguing spin ice[2] and multiferroic phenomena[3] which characterize some of these ground states.

The kagome lattice is comprised of a two-dimensional (2D) network of corner-sharing triangles. Several realizations of magnetic moments on stacked kagome lattices with varying degrees of crystalline order have been extensively studied. Recently studied examples include jarosites, such as $KFe_3(OH)_6(SO_4)_2$,[4] herbertsmithite $ZnCu_3(OH)_6Cl_2$,[5] and $Y_{0.5}Ca_{0.5}BaCo_4O_7$,[6] all of which show evidence of strong magnetic frustration.

The stacked kagome staircase materials $M_3V_2O_8$ (M =Ni,Co) display orthorhombic crystal structures with space group *Cmce*.[7] Their kagome layers are buckled and composed of edge-sharing $M^{2+}O_6$ octahedra. These layers are separated by nonmagnetic $V^{5+}O_4$ tetrahedra. The buckled kagome layers are perpendicular to the orthorhombic b axis and form what is known as a stacked kagome staircase structure. Figure 1(a) shows a single cobalt sublattice layer of the stacked kagome staircase structure, while Fig. 1(b) shows the projection of this layer of kagome staircase onto the a-c plane. The two inequivalent M sites are known as spines (M1) and cross ties (M2). The superexchange interaction between spine and cross-tie sites and between two adjacent spine sites are denoted by J_{sc} and J_{ss}, respectively.

One member of this family, $Ni_3V_2O_8$ (NVO), undergoes a series of phase transitions on lowering temperature.[8–12] A very interesting characteristic of this compound is that it exhibits simultaneous ferroelectric and incommensurate AFM order, that is, multiferroic behavior, in one of its ordered phases. In isostructural $Co_3V_2O_8$ (CVO), the $S=1$ magnetic moments at the Ni^{2+} site are replaced with $S=3/2$ Co^{2+} moments. CVO also displays a rich low-temperature phase diagram, which has been studied using polarized and unpolarized neutron diffraction,[13,14] dielectric measurements,[14] magnetization,[15,16] and specific-heat measurements.[16] There is a series of four AFM ordered phases below $T_N=11.3$ K

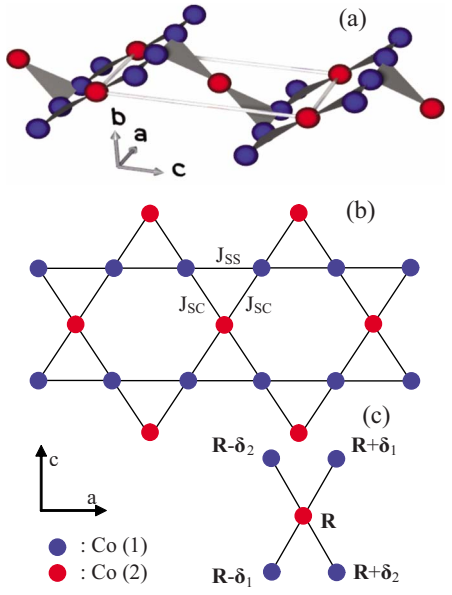

FIG. 1. (Color online) (a) A schematic diagram of the kagome staircase layer drawn in three dimensions (shown only for Co ions). The Co ions are represented by blue (dark gray) and red spheres (light gray) for spine (M1) and cross-tie (M2) sites, respectively. (b) The same structure shown in (a) as reduced to two dimensions in the a-c plane. (c) The basis used in the linear spin-wave theory calculation.

which can be characterized by incommensurate or commensurate ordering wave vectors $(0, \tau, 0)$. In contrast to NVO, the ultimate ground state in CVO is ferromagnetic and the Curie temperature is $T_C \sim 6$ K. Earlier powder neutron-diffraction measurements[14] on CVO showed ordered magnetic moments of 2.73(2) and 1.54(6)μ_B on the spine and cross-tie sites, respectively, at 3.1 K. All moments are aligned along the a-axis direction.

It is worth noting that the spine and cross-tie Co^{2+} sites in CVO are inequivalent, and thus these ions experience different crystalline electric fields, resulting in different unquenched orbital angular momentum. The unequal ordered moments on the spine and cross-tie Co^{2+} sites therefore have a different origin than the unequal ordered moments on different sublattices of the stacked triangular antiferromagnet $CsCoBr_3$.[17,18] This system displays a partially paramagnetic (PM) three sublattice Néel state where one of the three sublattices is disordered. This exotic state, in which very different ordered moments (zero and nonzero) are present on equivalent Co^{2+} sites, is a consequence of geometrical frustration.

While much work has been performed on the phase diagrams of NVO and CVO, little is known about the excitations, and correspondingly, the underlying microscopic spin Hamiltonian for these topical magnets. The ferromagnetic state in CVO is an excellent venue for such a study, as the ground state itself is very simple, and therefore the excitations out of the ground state should be amenable to modeling. In this paper we report inelastic neutron-scattering (INS) measurements of the spin-wave excitations within the kagome staircase plane in the FM ground state of single-crystal CVO. These measurements are compared with linear spin-wave theory which shows a surprising sublattice dependence to the exchange interactions.

II. EXPERIMENTAL DETAILS

A large (5 g) and high-quality single crystal of CVO was grown using an optical floating-zone image furnace. The dimensions of the crystal were roughly 12 mm in diameter and 22 mm in length. Heat capacity and magnetic measurements of this sample can be found elsewhere.[16]

Thermal INS measurements were performed at the Canadian Neutron Beam Centre at the Chalk River Laboratories using the C5 triple-axis spectrometer. A pyrolytic graphite (PG) vertically focusing monochromator and flat analyzer were used. Measurements were performed with a fixed final neutron energy of $E_f = 13.7$ meV and a PG filter in the scattered beam. The collimation after the monochromator was 29′-34′-72′, resulting in an energy resolution of 0.9 meV full width at half maximum (FWHM).

III. RESULTS

A. Magnetic inelastic neutron scattering

The crystal was oriented with the $(h0\ell)$ kagome staircase plane coincident with the scattering plane. Constant-**Q** energy scans were performed along the high-symmetry $(h00)$ and (00ℓ) directions in this plane. Figures 2(a) and 2(b) show

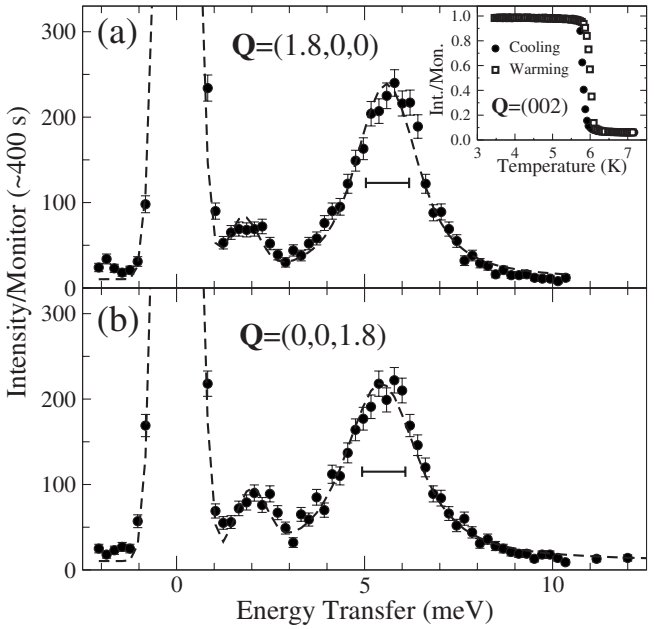

FIG. 2. Representative constant-**Q** INS spectra with (a) **Q** $=(1.8,0,0)$ and (b) (0, 0, 1.8) at $T=3$ K (FM phase). The broken line shows the resolution-corrected fits to the data, as described in text. The solid horizontal bars indicate the instrumental energy resolution. The inset shows heating and cooling scans of the (mainly) magnetic elastic (002) Bragg scattering, which is characteristic of the FM ground state in CVO.

representative constant-**Q** scans at $T=3$ K and **Q** $=(1.8,0,0)$ and (0,0,1.8), respectively. The (002) nuclear Bragg peak is very weak and is coincident with a strong FM Bragg peak below T_C. The inset of Fig. 2(a) shows the temperature dependence of this Bragg reflection on independent warming and cooling runs. An abrupt falloff in intensity near $T_C \sim 6$ K and accompanying hysteresis indicate the strongly discontinuous nature of this phase transition.

The overall features of the two spectra in Fig. 2 are quantitatively similar at $T=3$ K. Two spin-wave excitations, identified on the basis of their temperature and Q dependencies, are observed and have been modeled using resolution-convoluted damped harmonic-oscillator (DHO) line shapes.[19] The resulting fits are shown as the dashed lines in Fig. 2, and this analysis allows us to conclude that the higher-energy spin wave, near 5.7 meV in both cases, has a substantial intrinsic energy width of $\Gamma = 0.70(8)$ meV at **Q** $=(1.8,0,0)$ and 0.90(8) meV at **Q**$=(0,0,1.8)$.

A series of constant-**Q** scans for $(h00)$ and (00ℓ) directions were collected at $T=3$ K and are presented as a color contour map in Figs. 3(a) and 3(c). Dispersive features corresponding to two bands of spin waves are seen in both data sets. The top of the upper spin-wave band at $\Delta E \sim 5.7$ meV corresponds to excitations reported earlier using a time-of-flight technique.[10] These constant-**Q** scans were fit to resolution-convoluted DHO line shapes. Examples of these fits at $T=3$ K are shown by the dashed lines in Figs. 4(a) and 4(b) wherein constant-**Q** scans at **Q**$=(3.4,0,0)$ are shown along with the fits on both linear [Fig. 4(a)] and logarithmic [Fig. 4(b)] intensity scales. These results gave intrinsic energy widths for the higher-energy spin-wave mode at

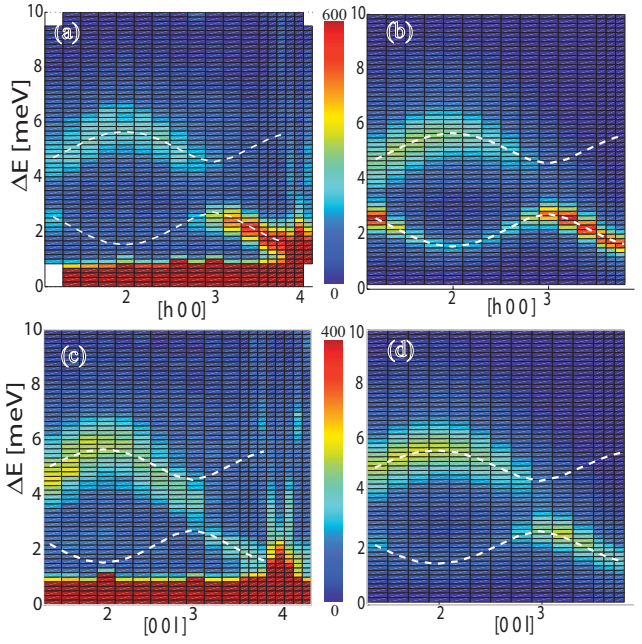

FIG. 3. (Color) [(a) and (c)] Color contour maps of INS at $T=3$ K and [(b) and (d)] corresponding linear spin-wave theory as described in the text. The broken lines show the dispersion relations resulting from this spin-wave theory analysis.

all wave vectors ranging from $\Gamma=0.6$ to 1.1 meV, while the lower-energy spin waves were resolution limited at all wave vectors. This indicates a finite lifetime for the higher-energy spin waves even at temperatures $\sim T_C/2$.

The spin-wave spectrum evolves rapidly with increasing temperature. Figure 4(a) shows $\mathbf{Q}=(3.4,0,0)$ scans at $T=3$ K (FM phase) and 20 K (well into the PM phase). In the FM phase there is a prominent spin-wave peak at $\Delta E=2.0$ meV. A higher-energy spin-wave peak is also present in this scan but with a much lower peak intensity and an intrinsic energy width of $\Gamma=0.9$ meV. At 20 K the well-defined low-energy spin wave has disappeared and only broad low-ΔE scattering remains. The inset of Fig. 4(a) shows the temperature dependence of spin-wave peak intensity at $\Delta E=2.0$ meV in the neighborhood of T_C. The same rapid falloff, as was seen in the magnetic Bragg scattering at (002), is also seen in the inelastic intensity, as well as the same hysteresis, indicating that these spin waves are strongly coupled to the ferromagnetic order parameter.

Figure 4(c) shows the same constant-$\mathbf{Q}$ scans as in Fig. 2 but now at 20 K rather than 3 K. The well-defined spin-wave modes are no longer present, and the low-energy inelastic scattering is significantly greater at $\mathbf{Q}=(0,0,1.8)$ as compared with (1.8, 0, 0) at $T=20$ K. The temperature dependence of this scattering is contrasted in the inset of Fig. 4(c). The $\mathbf{Q}=(1.8,0,0)$ inelastic scattering drops quickly at $T_C\sim 6$ K while that at $\mathbf{Q}=(0,0,1.8)$ gradually increases with temperature. We attribute this difference to prominent longitudinal easy-axis spin fluctuations along the a axis at high temperatures. Given that the neutron-scattering cross section[19] is sensitive to magnetic fluctuations perpendicular to $\mathbf{Q}$, longitudinal fluctuations would be seen in the $\mathbf{Q}=(0,0,1.8)$ spectrum rather than the (1.8,0,0) spectrum. Note

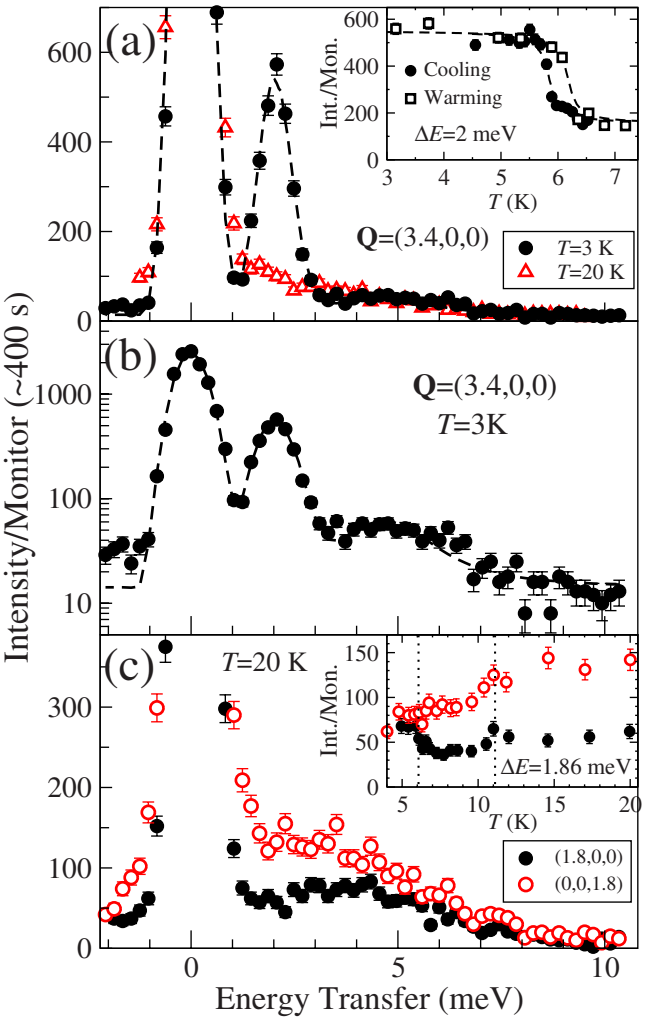

FIG. 4. (Color online) (a) INS scans at $\mathbf{Q}=(3.4,0,0)$ for $T=3$ and 20 K. The inset shows the temperature dependence of the scattering at the inelastic peak position. The lines in the inset are guides to the eyes. (b) The same data in panel (a) and DHO fits with log intensity axis. (c) Scans in the PM phase for $\mathbf{Q}=(1.8,0,0)$ and (0, 0, 1.8). The inset (same legend as main figure) shows the temperature dependence of the inelastic scattering at the spin-wave peak (for $T=3$ K, see Fig. 2) at $\Delta E=1.86$ meV for the different $\mathbf{Q}$ directions. The vertical dotted lines in the inset indicate T_C and T_N.

that the highest temperature transition to the paramagnetic state at $T_N=11.3$ K is evident as a change in slope of the temperature dependence shown in the inset of Fig. 4(c), and both $T_C\sim 6$ K and $T_N=11.3$ K are indicated by dashed vertical lines in this inset.

B. Spin-wave theory calculations

We have carried out a linear spin-wave theory analysis of the magnetic excitations observed in Figs. 3(a) and 3(c) to understand the relevant microscopic spin Hamiltonian as much as possible. The full Hamiltonian is potentially complicated if account is taken of the three-dimensional (3D) kagome staircase structure. We employed a 2D model in which the magnetic ions in a layer are projected onto the

average plane of the layer (Fig. 1) and only near-neighbor exchange and single-ion anisotropy are included.

We change from the conventional centered-rectangular unit cell to a primitive rhombohedral unit cell defined by lattice vectors $\mathbf{R}_1=(\frac{a}{2},\frac{c}{2})$ and $\mathbf{R}_2=(\frac{a}{2},-\frac{c}{2})$ and basis vectors $\boldsymbol{\delta}_1=\mathbf{R}_1/2$, $\boldsymbol{\delta}_2=\mathbf{R}_2/2$, and $\boldsymbol{\delta}_3=0$. If $\mathbf{R}$ describes the set of lattice points and $\mathbf{S}_\mathbf{r}$ is the spin operator at a location $\mathbf{r}$, we can write

$$\mathcal{H}_{\rm sc}=-J_{\rm sc}\sum_{\mathbf{R}}\sum_{\boldsymbol{\delta}=\pm\boldsymbol{\delta}_1,\pm\boldsymbol{\delta}_2}\mathbf{S}_\mathbf{R}\cdot\mathbf{S}_{\mathbf{R}+\boldsymbol{\delta}}, \tag{1}$$

$$\mathcal{H}_{\rm ss}=-J_{\rm ss}\sum_{\mathbf{R}}[\mathbf{S}_{\mathbf{R}+\boldsymbol{\delta}_1}\cdot\mathbf{S}_{\mathbf{R}-\boldsymbol{\delta}_2}+\mathbf{S}_{\mathbf{R}-\boldsymbol{\delta}_1}\cdot\mathbf{S}_{\mathbf{R}+\boldsymbol{\delta}_2}]. \tag{2}$$

$\mathcal{H}_{\rm sc}$ and $\mathcal{H}_{\rm ss}$ are the exchange interactions between spine and cross-tie spins with couplings $J_{\rm sc}$ and $J_{\rm ss}$. The fact that the spine and cross-tie spins are found to be ferromagnetically aligned implies that $J_{\rm sc}$ is positive. We choose the spin z axis parallel to the crystallographic a axis, consistent with the ordered moment direction. Magnetization measurements have established that the crystallographic b axis (spin x axis) is a harder axis than the c axis (spin y axis).[15,16] The appropriate single-ion anisotropy Hamiltonian $\mathcal{H}_a$ distinguishes the three orthogonal directions and the inequivalent sites

$$\mathcal{H}_a=\sum_{\mathbf{R}}\sum_{i=1,2,3}\sum_{\alpha=x,y,z}A_i^\alpha(S^\alpha_{\mathbf{R}+\boldsymbol{\delta}_i})^2. \tag{3}$$

The sequence from hard to easy axis is established by the condition $A_i^x>A_i^y>A_i^z$. We use the reduced anisotropies $\Delta_i=(A_i^x+A_i^y-2A_i^z)/2$ and $\epsilon_i=(A_i^x-A_i^y)/2$. Since the $i=1$ and 2 sites are equivalent there are four independent parameters Δ_s, Δ_c, ϵ_s, and ϵ_c.

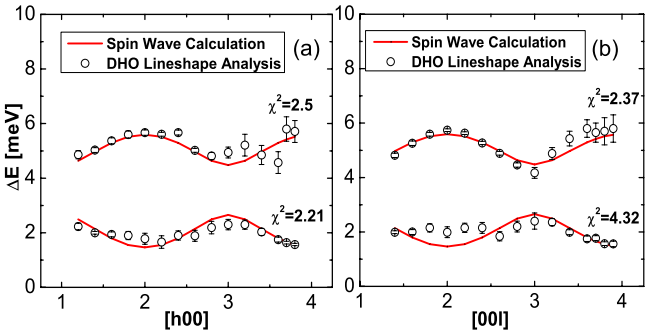

FIG. 5. (Color online) Comparison between the measured spin-wave energies, as determined by fitting neutron groups to DHO line shapes, and the results of the spin-wave theory calculation, as described in text. The spin-wave theory results have been fitted to the experiment, both of which are shown along the $[h00]$ and $[00l]$ scattering directions in panels (a) and (b), respectively.

In linear spin-wave theory[20] the total Hamiltonian $\mathcal{H}$ may be written in terms of spin-wave operators $c_i(\mathbf{k})$ and $c_i^\dagger(\mathbf{k})$

$$\mathcal{H}=\sum_{\mathbf{k},i,j}h_{ij}(\mathbf{k})c_i^\dagger(\mathbf{k})c_j(\mathbf{k})+\frac{1}{2}\sum_{\mathbf{k},i,j}g_{ij}(\mathbf{k})[c_i^\dagger(\mathbf{k})c_j^\dagger(-\mathbf{k})+c_j(-\mathbf{k})c_i(\mathbf{k})], \tag{4}$$

$$h(\mathbf{k})=2S\begin{pmatrix}J_{\rm sc}+J_{\rm ss}+\Delta_s & -J_{\rm ss}\cos\mathbf{k}\cdot(\boldsymbol{\delta}_1+\boldsymbol{\delta}_2) & -J_{\rm sc}\cos\mathbf{k}\cdot\boldsymbol{\delta}_1\\ -J_{\rm ss}\cos\mathbf{k}\cdot(\boldsymbol{\delta}_1+\boldsymbol{\delta}_2) & J_{\rm sc}+J_{\rm ss}+\Delta_s & -J_{\rm sc}\cos\mathbf{k}\cdot\boldsymbol{\delta}_2\\ -J_{\rm sc}\cos\mathbf{k}\cdot\boldsymbol{\delta}_1 & -J_{\rm sc}\cos\mathbf{k}\cdot\boldsymbol{\delta}_2 & 2J_{\rm sc}+\Delta_c\end{pmatrix},\quad g(\mathbf{k})=2S\begin{pmatrix}\epsilon_s & 0 & 0\\ 0 & \epsilon_s & 0\\ 0 & 0 & \epsilon_c\end{pmatrix}, \tag{5}$$

where $i,j=1,2,3$. Although the moments on the different sites are unequal our analysis uses $S=3/2$ for all sites. This is not an unphysical assumption, however, as the differing ordered moments can simply be incorporated into the exchange and anisotropy constants, as it is the product of ordered moment and coupling constants which appears in all calculations.

The unpolarized magnetic neutron-scattering cross section and the spin-spin correlation functions it contains can be related to one spin-wave Green's functions. The Green's functions can be calculated by inverting a matrix involving the two matrices, $h(\mathbf{k})$ and $g(\mathbf{k})$ defined above, following Coll and Harris.[21] The spin-wave energies are determined by solving for the zeros of a determinant involving matrix elements of the inverse Green's function. The resulting scattering function $\mathcal{S}(\mathbf{Q},\Delta E)$ for $\mathbf{Q}$ parallel to (00ℓ) is proportional to

$$\mathcal{S}(\mathbf{Q},\Delta E)\propto\sum_{i,j}{\rm Im}[(h-g)(z^2I-h^2+g^2+hg-gh)^{-1}]_{i,j}, \tag{6}$$

where I is the identity matrix, $\mathbf{k}=\mathbf{Q}$, $z=\Delta E-i\Gamma$ is the complex energy, and i and j are summed over the indices of the 3×3 matrix in square brackets. The expression for $\mathbf{Q}$ parallel to $(h00)$ has a similar form. The resulting scattering functions are multiplied by the magnetic form factor, the Bose factor, and a single intensity scale factor and are plotted in Figs. 3(b) and 3(d). Note that the calculation gives three spin-wave modes for each $\mathbf{Q}$ where one of the three carries no intensity.

Best agreement between the experimental data and the spin-wave theory calculation in Fig. 3 was obtained for magnetic coupling predominantly between the spine and cross-tie Co ions with $J_{\rm sc}=1.25\pm0.08$ meV, while the spine-spine

coupling J_{ss} vanishes. The best-fit spin-wave uniaxial anisotropy parameters are $\Delta_s=1.5\pm0.1$ meV, $\Delta_c=2.13\pm0.2$ meV, $\epsilon_s=0.6\pm0.3$ meV, and $\epsilon_c=1.2\pm0.3$ meV.

Figure 3 shows that the spin-wave theory gives a very good description of the dispersion of the two modes (dashed lines) and accounts for the observed trend of the spin waves to trade intensity as a function of **Q**. The calculation is not convolved with the instrumental resolution; instead the energy width is manually set in both high- and low-energy bands to correspond to the measured width. The broad (in energy) neutron groups corresponding to the upper spin-wave bands are most evident near (200) and (002). The lower-energy spin-wave band becomes much more intense near the zone centers of (400) and (004).

While the description of the experimental spin-wave spectrum by the theory is very good, it is not perfect. The calculated dispersion of the lower spin-wave band is low compared with experiment near (200) and (002) where the intensity is very weak. This can be seen more clearly in Fig. 5, which compares the experimental and calculated spin-wave energies as a function of **Q**. The goodness-of-fit, χ^2, values for each of the upper- and lower-energy spin-wave bands are given in Fig. 5. This shows the dispersion of the broad upper spin-wave band to be well accounted for, while the dispersion of the lower band has discrepancies between theory and experiment of about ~0.6 meV at certain wave vectors. This energy difference is similar to the dispersion observed along the stacking direction (**b**) by earlier neutron measurements,[10] and we conjecture that it likely originates from weak three-dimensional exchange coupling along the $(0,k,0)$ or stacking direction, which is beyond the scope of our calculation.

C. Phonon scattering

Steep excitation branches near (400) and (004) with comparatively weak intensity [Figs. 3(a) and 3(c)] are identified as longitudinal-acoustic phonons, with a corresponding speed of sound of 1050 ± 100 m/s, in both directions. These dispersive excitations are observed at temperatures well beyond $T_N=11.3$ K and scale in intensity with the structure factor, as expected of acoustic phonons. Phonons and their potential coupling to the spin system have been of some appreciable interest in both CVO and NVO. A strong dielectric anomaly in CVO at $T_C\sim6$ K for $\mathbf{E}\|(00l)$ has been reported[14] and this can be interpreted in terms of strong spin-lattice coupling. More recently, however, an energy-dependent magneto-optical study[22] has shown that CVO displays relatively weak magnetodielectric behavior compared to that seen in NVO, suggesting that spin-lattice coupling in CVO is not particularly strong at low temperatures. Our results show conventional behavior for the low-lying longitudinal-acoustic phonons, and further study would be required to investigate potential manifestation of spin-lattice coupling in CVO.

IV. CONCLUSION

To conclude, our INS study of the spin-wave excitations in the ferromagnetic ground state of CVO within its kagome staircase plane reveals two separate spin-wave bands with energies between 1.6 and 5.7 meV. The upper spin-wave band is damped with finite-energy widths Γ in the range of 0.6–1.1 meV. These spin-wave excitations can be accurately described by a simple model Hamiltonian and linear spin-wave theory. The model gives magnetic coupling that is predominantly between the spine and cross-tie sites of the kagome staircase.

ACKNOWLEDGMENT

This work was supported in part by NSERC of Canada.

[1] *Frustrated Spin Systems*, edited by H. T. Diep (World Scientific, Singapore, 2004).
[2] S. T. Bramwell and M. J. P. Gingras, Science **294**, 1495 (2001).
[3] T. Kimura, T. Goto, H. Shintani, K. Ishizaka, T. Arima, and Y. Tokura, Nature (London) **426**, 55 (2003); N. A. Hill, J. Phys. Chem. B **104**, 6694 (2000).
[4] K. Matan, D. Grohol, D. G. Nocera, T. Yildirim, A. B. Harris, S. H. Lee, S. E. Nagler, and Y. S. Lee, Phys. Rev. Lett. **96**, 247201 (2006); D. Grohol, K. Matan, J. H. Cho, S. H. Lee, J. W. Lynn, D. G. Nocera, and Y. S. Lee, Nature Mater. **4**, 323 (2005).
[5] J. S. Helton, K. Matan, M. P. Shores, E. A. Nytko, B. M. Bartlett, Y. Yoshida, Y. Takano, A. Suslov, Y. Qiu, J.-H. Chung, D. G. Nocera, and Y. S. Lee, Phys. Rev. Lett. **98**, 107204 (2007).
[6] W. Schweika, M. Valldor, and P. Lemmens, Phys. Rev. Lett. **98**, 067201 (2007).
[7] E. E. Sauerbrei, R. Faggiani, and C. Calvo, Acta Crystallogr., Sect. B: Struct. Crystallogr. Cryst. Chem. **29**, 2304 (1973).
[8] M. Kenzelmann, A. B. Harris, A. Aharony, O. Entin-Wohlman, T. Yildirim, Q. Huang, S. Park, G. Lawes, C. Broholm, N. Rogado, R. J. Cava, K. H. Kim, G. Jorge, and A. P. Ramirez, Phys. Rev. B **74**, 014429 (2006).
[9] G. Lawes, M. Kenzelmann, N. Rogado, K. H. Kim, G. A. Jorge, R. J. Cava, A. Aharony, O. Entin-Wohlman, A. B. Harris, T. Yildirim, Q. Z. Huang, S. Park, C. Broholm, and A. P. Ramirez, Phys. Rev. Lett. **93**, 247201 (2004).
[10] N. R. Wilson, O. A. Petrenko, G. Balakrishman, P. Manuel, and B. Fak, J. Magn. Magn. Mater. **310**, 1334 (2007).
[11] N. Rogado, G. Lawes, D. A. Huse, A. P. Ramirez, and R. J. Cava, Solid State Commun. **124**, 229 (2002).
[12] T. Lancaster, S. J. Blundell, P. J. Baker, D. Prabhakaran, W. Hayes, and F. L. Pratt, Phys. Rev. B **75**, 064427 (2007).
[13] N. R. Wilson, O. A. Petrenko, and L. C. Chapon, Phys. Rev. B **75**, 094432 (2007).
[14] Y. Chen, J. W. Lynn, Q. Huang, F. M. Woodward, T. Yildirim, G. Lawes, A. P. Ramirez, N. Rogado, R. J. Cava, A. Aharony, O. Entin-Wohlman, and A. B. Harris, Phys. Rev. B **74**, 014430 (2006).
[15] G. Balakrishnan, O. Petrenko, M. R. Lees, and D. McK. Paul, J. Phys.: Condens. Matter **16**, L347 (2004).
[16] R. Szymczak, M. Baran, R. Diduszko, J. Fink-Finowicki, M.

Gutowska, A. Szewczyk, and H. Szymczak, Phys. Rev. B **73**, 094425 (2006).
[17] M. Mao, B. D. Gaulin, R. B. Rogge, and Z. Tun, Phys. Rev. B **66**, 184432 (2002).
[18] J. van Duijn, B. D. Gaulin, M. A. Lumsden, J. P. Castellan, and W. J. L. Buyers, Phys. Rev. Lett. **92**, 077202 (2004).
[19] G. Shirane, S. M. Shapiro, and J. M. Tranquada, *Neutron Scattering with a Triple-Axis Spectrometer* (Cambridge University Press, Cambridge, 2002), p. 47.
[20] T. Holstein and H. Primakoff, Phys. Rev. **58**, 1098 (1940).
[21] C. F. Coll III and A. B. Harris, Phys. Rev. B **4**, 2781 (1971).
[22] R. C. Rai, J. Cao, L. I. Vergara, S. Brown, J. L. Musfeldt, D. J. Singh, G. Lawes, N. Rogado, R. J. Cava, and X. Wei, Phys. Rev. B **76**, 174414 (2007).